PAPER

Check for updates

Molten salt synthesis of increased (100)-facet and polycrystalline nickel oxide nanoparticles for the oxygen evolution reaction: impact of facet and crystallinity on electrocatalysis†

Darius W. Hayes,[ae] Elliot Brim, [iD][a] Konstantin Rücker, [iD][bc] Dereje Hailu Taffa, [iD][c] Omeshwari Bisen, [iD][d] Marcel Risch, [iD][d] Shaun M. Alia,[e] Jullian Lorenz, [iD][b] Corinna Harms,[b] Michael Wark [iD][c] and Ryan M. Richards [iD]*[ae]

Nickel oxide nanocubes with increased (100) surface facet presence (NiO(100)) were synthesized through a molten salt synthesis procedure to probe their oxygen evolution reaction (OER) activity in order to investigate the relationship between the surface facet and OER performance. While altering the synthesis parameters to decrease NiO(100) particle sizes and agglomeration, a polycrystalline NiO nanoparticle system formed from using Li_2O as a Lux–Flood base (labelled Li_2O-MSS NiO, where MSS stands for molten salt synthesis). This novel synthesis was further elaborated and the obtained materials were also tested for OER activity. After thorough structural characterization to determine crystallinity, lattice spacings, and elemental distribution, their OER activity was compared *versus* high surface area NiO(111) nanosheets in a three-electrode rotating disk electrode (RDE) system. The activity trend of (111) > Li_2O-MSS > (100) was observed. This decrease in activity of the nanocube and polycrystalline samples was explained by differences between theoretical and experimental conditions, differences in ink rheology and resulting catalyst layer properties, and significant agglomeration seen in the imaging of the sample. Methods for improving the OER activity of these samples are discussed in the conclusion of this study.

Introduction

Hydrogen is a promising emerging technology in energy and storage. Currently, the bulk of hydrogen is produced through steam methane reforming and coal gasification processes due to cost. Water electrolysis is an alternative hydrogen production process at a feasible cost.[1] This process consists of two electrochemical reactions: the hydrogen evolution reaction (HER) that occurs at the cathode of an electrochemical cell, and the oxygen evolution reaction (OER), which occurs at the anode.[2] Due to being a four-electron

transfer process, the OER demonstrates sluggish kinetics and thus much effort is placed in the search for electrocatalysts for this reaction.

The current standards of OER electrocatalysts are platinum group metal (PGM) based catalysts such as iridium oxide (IrO_2) used in acidic media;[3] however, the rarity of these metals leads to them being prohibitively expensive as catalysts on an industrial scale. To counter this, alkaline media-based electrolyzers are being studied to allow the use of transition metal oxide (TMO) based catalysts in different structures such as spinels, layered double hydroxides, and perovskites.[4] Emphasis has been put on the development of anion exchange membrane (AEM) electrolyzers due to their advantages in improved cell efficiency compared to traditional alkaline electrolyzers, PGM-free components, and improved stability at high pH. Rock salt structured TMOs are promising materials to study OER electrocatalysis due to their simple structure. Nickel oxides in particular have experimentally shown promising OER activity.[5–7] Computational studies indicate that nickel oxide with the (100) surface facet should possess OER activity comparable to PGM catalysts;[8] however, NiO(100) is not thermodynamically stable *via* the wet chemical synthesis routes that have been

[a] Department of Chemistry, Colorado School of Mines, 1500 Illinois St., Golden, Colorado 80401, USA. E-mail: rrichard@mines.edu
[b] Institute of Engineering Thermodynamics, German Aerospace Center (DLR), Carl-von-Ossietzky-Str. 15, 26129 Oldenburg, Germany
[c] Institute of Chemistry, Chemical Technology I, Carl von Ossietzky University of Oldenburg, Carl-von-Ossietzky-Str. 9-11, 26129 Oldenburg, Germany
[d] Nachwuchsgruppe Gestaltung des Sauerstoffentwicklungsmechanismus, Helmholtz-Zentrum Berlin für Materialien und Energie GmbH, Hahn-Meitner-Platz 1, 14109 Berlin, Germany
[e] Chemical and Material Sciences Center, National Renewable Energy Laboratory, 15013 Denver W Pkwy, Golden, Colorado, 80401, USA
† Electronic supplementary information (ESI) available. See DOI: https://doi.org/10.1039/d5lf00072f

previously established.[9] Studies of thin films produced from current-sputtering have indicated that NiO(100) is the least active facet.[10] Here, we investigate the production of NiO(100) *via* molten salt synthesis and their electrochemical OER evaluation. This initial synthesis, however, resulted in a significantly agglomerated product; thus, alternative synthetic routes to produce non-agglomerated NiO(100) nanocubes were investigated. A subsequent synthesis route was developed using Li_2O as a Lux–Flood base to reduce nanoparticle size,[11] yielding a polycrystalline product. This new polycrystalline NiO (labelled Li_2O-MSS NiO) was tested for OER catalytic activity as well to provide further insights into the relationship between physical/crystalline properties and OER activity.

Methods

Molten salt synthesis of NiO(100)

Cubic nickel oxide nanoparticles were synthesized through decomposition of $Ni(NO_3)_2·6H_2O$ precursor in a 1 : 1 mixture of KNO_3 and $NaNO_3$ molten salts. 1.00 g (and in later iterations, 2.00 g) of $Ni(NO_3)_2·6H_2O$ precursor was added to the $KNO_3/NaNO_3$ mixture in an (initially) 1 : 10 molar ratio of precursor to salt.[12] This powder mixture was ground by a mortar and pestle then placed into a tube furnace in glass sample holders to be heated up to a range of calcination temperatures from 300 to 550 °C at a heating rate of 2.5 °C per minute. The heating occurred under dry air flow at a rate of 500 cc per minute. Initial synthesis held the sample at the max. calcination temperature for 1 h before cooling back to room temperature, however this step was eventually removed (as discussed in the Results section). After cooling to room temperature, the product received from the tube furnace is a solid block of mixed white dried molten salts and either a green solid product at lower temperatures or a darker grey to black solid product at higher temperatures. This product is dissolved in an approximate 1 : 1 solution mixture of ethanol and water until all product is fully in solution, followed by washing and drying with vacuum filtration set-up until the final powder product is recovered. This powder is vacuum dried at 120 °C overnight then collected for characterization.

Molten salt synthesis of NiO with lithium oxide reducing agent

A modified version of the existing molten salt synthesis was developed based on a low temperature metal oxide synthesis using Li_2O as a reducing agent.[11] Here, the initial steps taken in the previous synthesis were followed with 0.21 g of Li_2O powder added to the mixture of powders. The product was heated in the same temperature range as the initial synthesis under the same ramp rate and flow rate of dry air. Calcination yielded a darker black product and the same washing and drying procedure with vacuum filtration was followed. No vacuum drying was done on these samples.

Solvothermal high pressure synthesis of NiO(111)

Previous work described a solvothermal synthesis route for high surface area NiO nanosheets with (111) surface facets.[13,14] This was accomplished through dissolving $Ni(NO_3)_2·6H_2O$ precursor in methanol with benzyl alcohol (as the structure directing agent for the (111) facet) and urea with stirring for 1 h or until fully dissolved. The solution was then placed in a 600 mL autoclave, purged with Ar and pressurized to 9 bar, then finally heated to 200 °C then 265 °C to reach the pseudo-supercritical drying point of the methanol solution. At the desired time, methanol vapor was released, leaving behind a light green powder indicative of $Ni(OH)_2$. Finally, the $Ni(OH)_2$ powder is calcined at 400 °C (ref. 14) to produce NiO(111) in a fine dark grey powder form.

Characterization techniques

XRD. Product crystallinity, crystal pattern, and phase pattern analysis was conducted by powder X-ray diffraction (pXRD) on a Bruker D2 Phaser Benchtop XRD instrument with a Cu radiation source. Samples were measured between the range of 20–85 2θ degrees. The Scherrer equation was employed by the DIFFRAC.EVA program for crystallite size analysis.

TEM. Imaging and lattice spacing (*d*-spacing) analysis of products were done by high resolution transmission electron microscopy (HRTEM) on an FEI Talos F200X TEM. High resolution imaging was done at 200 kV with the sample placed on copper grids with carbon support mesh. Samples were sonicated in methanol then drop cast onto the grids at least one hour prior to analysis. Lattice spacing analysis was done by measuring the distance between lattice fringes using the high-resolution magnitude range (500k×). ImageJ was used to calibrate according to the given scale bar of the instrument and measure the distance across ten lattice fringes. The value obtained from this measurement was divided by ten to obtain the average *d*-spacing measurement. This measurement was done through multiple regions of the sample image to confirm facet exposure through the sample. Scanning transmission electron microscopy (STEM) mode was activated to use energy dispersive spectroscopy (STEM-EDS) to generate an elemental distribution map of samples.

XAS. X-ray absorption spectroscopy (XAS) experiments were conducted on samples at the Ni K-edge using the KMC-2 beamline at the BESSY II electron storage ring (300 mA, top-up mode) operated by Helmholtz-Zentrum Berlin für Materialien und Energie in Berlin, Germany.[15] Further details of the experimental setup are described elsewhere in detail.[16] X-ray Absorption Near Edge Spectroscopy (XANES) was used to determine the bulk oxidation state of the materials while Extended X-Ray Absorption Fine Structure (EXAFS) was used for local environment and bonding information on the sample. XAS analysis was done on NiO(100) and NiO(111) samples prepared through two different preparation techniques including measuring thin film (tf) samples of

catalyst ink deposited on glassy carbon surfaces and catalyst powder (cp) samples prepared by spreading a thin homogeneous layer of powder on Kapton tape and folding into 1×1 cm^2. Finally, thin film samples with additional electrochemical treatment (tf-pd) samples were also measured. The NiO(100) and NiO(111) samples were measured in the fluorescence mode, setting the sample at a 45° to the Si photodiodes and the reference Ni metal foil in transmission configuration in front of an ionization chamber detector. The commercial reference Ni-oxides (NiO_ROTH and LiNiO$_2$) were measured in transmission mode using ion chambers. The XAS energy was calibrated by setting the first inflection point of a simultaneously measured Ni foil to 8333 eV. Normalization of all spectra involved the subtraction of a straight line obtained by fitting the data before the K-edge and division by a polynomial function obtained by fitting the data after the K-edge. The edge position was determined as the integral under the normalized XANES spectra with the integral limit of $\mu_1 = 0.15$ and $\mu_2 = 1$. EXAFS analysis was conducted by generating a Fourier Transform (FT) between 35 and 550 eV above the Ni K-edge, with an E_0 value of 8333 eV for Ni.

Electrochemical characterization

The OER electrode activity of samples was determined through electrochemical measurements conducted by three-electrode experiments using a rotating disc electrode (RDE) with the Pine Research Instrumentation, AFMSRCE modulated rotator. The RDE set-up consists of an Au substrate surrounded by a PTFE shroud for the working electrode (0.196 cm^2, Pine Research Instrumentation, AFE5T050AU) with a catalyst suspension drop cast on the electrode surface; a Au wire with a mesh was used as the counter electrode; a Hg/HgO electrode (in 20% w/w KOH) was used as the reference electrode in a PTFE cell and Autolab PGSTAT302N potentiostat (Eco Chemie, Metrohm Autolab).[1] Au substrate electrodes were used due to the increased stability compared to carbon substrate electrodes and the lack of OER activity in the linear sweep voltammetry region of interest.[17] The catalyst ink was prepared by weighing out 4.0 mg of catalyst powder and dispersing in 1500 μL of DI water and 400 μL of isopropanol. After chilling with an ice bath (5 min) and ultrasonicating with a horn sonicator (30 s), 9.04 μL Nafion was added as a binder followed by another 10 minutes of horn sonication while in an ice bath. This ink formula (labelled Ink Formula B in the ESI†) corresponds to a catalyst loading of 100 μg cm^{-2}. Once the binder was added, the catalyst ink was ultrasonicated with the horn sonicator for 10 minutes to ensure proper dispersion of the catalyst powder in the ink; when the catalyst powder would settle in solution after lengthy amounts of time (such as days between experiments), the ink would be chilled and ultrasonicated again to ensure all electrodes were made under the same ink conditions. The ink was drop-cast onto the Au substrate electrodes and rotated at 750–800 RPM in atmospheric air until a uniform thin film covered the electrode. 0.1 M NaOH (Sigma Aldrich, TraceSelect, 99.9995%) solution is used as an electrolyte that is bubbled with N$_2$ gas for at least ten minutes prior to every voltammetry experiment. A reference correction value is subtracted from the intended potential window of experiments to account for the potential range *versus* reversible hydrogen electrode (RHE). This was determined through a reference correction measurement taken at the beginning of every day using a Pt working electrode in a NaOH electrolyte solution bubbled with H$_2$ gas for at least ten minutes. The reference correction value was taken from the cyclic voltammogram (CV) of this set-up, with the correction value being taken at the potential where the current crosses the *X*-axis. The exact reference correction values are shown in Table S7,† where the different reference values correspond to the different days the experiment was done (each sample was tested on a different day due to experiment timing). The exact reference correction value of each day of experiments was used for reference correction in the post-experiment data analysis of all RDE experiment results for accurate correction of Hg/HgO to RHE. Linear sweep voltammetry (LSV) measurements are conducted by completing five cycles at 100 mV s^{-1} scan rate at the start of a measurement followed by a linear sweep scan at 10 mV s^{-1} scan rate. LSV measurements are done in a shortened potential range in the kinetic range of the OER (∼1.2–1.8 V *vs.* RHE) and the full OER potential range (∼1.2–2.0 V). Cyclic voltammetry was done in the wider potential range of ∼0–1.75 V *vs.* RHE. CVs were used to determine changes in both current density and redox potentials to elucidate redox changes. The electrode activities of both LSVs and CVs were compared through normalizing the current by metal oxide catalyst mass (mass activity), the area of the electrode which was 0.196 cm^2 (current density),[1] and through electrochemical surface area (ECSA) values determined through double layer capacitance measurements, which are described towards the end of this section. ECSA values were obtained by dividing the measured double layer capacitance values by specific capacitance, which is assumed to be 40 μF cm^{-2}.[18] Electrochemical impedance spectroscopy (EIS) measurements are also done to determine uncompensated solution resistance (R_u) and charge transfer resistance in the frequency range of 1 Hz to 100 kHz with an AC amplitude of 10 mV at the open circuit potential (typically in the range of ±0.2 V *vs.* Hg/HgO). The open circuit potential is automatically determined by the potentiostat before frequency response analysis (FRA) measurements are taken. The R_u is taken at the start of the FRA measurement in the 100 kHz range. EIS measurements were run at the very beginning of the experiment before capacitance measurements (the beginning of the procedure) and after all CV and LSV measurements were completed, preceding the final capacitance measurement. Once an EIS measurement was completed, the R_u was extracted to manually *iR* correct the data of all LSV and CV trials during post-experiment data analysis by multiplying the measured current (A) with the measured R_u (Ω) to calculate the *iR* drop. The Nyquist plots derived from these EIS measurements are shown in Fig. S13.†

The average R_u of each sample across the reported trials is shown in Table S6.† The iR drop is then subtracted from the applied potential to determine the iR-corrected potential. Current values through different normalizations (mass activity, current density, specific activity) were then plotted against this manually iR-corrected potential. Manual iR corrections were done to both ensure accuracy and due to the inability to use in situ automatic iR correction and automatic current ranging at the same time on the potentiostat used for testing. Capacitance measurements were used to determine double layer capacitance for calculating approximate ECSA values. Capacitance measurements were conducted from the potential range of −0.1 to 0.15 V vs. Hg/HgO reference (0.75 to 1.0 V vs. RHE) at scan rates of 8 mV s^{-1} (~10 mV s^{-1}), 50 mV s^{-1}, 100 mV s^{-1}, 500 mV s^{-1}, 1 V, 5 V s^{-1}, and 10 V s^{-1} with step sizes of 1 V except for 5 and 10 mV which were increased to 5 V step sizes. However, the potential with this method in terms of accurately measuring capacitance for low conductive metal oxide catalysts is discussed later.[14,18] Though turnover frequency (TOF) is a commonly used parameter for OER characterization,[19] the TOF of the NiO systems could not be extracted due to the overlap of the Ni$^{2+/3+}$ peak and the Au oxidation peak. As such, one should keep in mind that the ECSA-normalized trends seen based on the capacitance studies may reflect active-site density alongside intrinsic kinetics.

Results and discussion

X-ray diffraction was used on powder samples after washing and drying. Additionally, different washing steps (such as using different dissolution solvents and the impact of vacuum drying) were performed on the 400 °C sample to investigate the impact on crystallinity (as described in the ESI†). XRD (Fig. 1a) confirmed the crystallinity of initial molten salt synthesis samples with strong peaks present at the 2θ values of 37.5°, 44.5°, 64°, 75.4°, and 79.3°. These peaks correspond to the (111), (002), (220), (411), and (222) crystal planes of the face-centered cubic rock salt structure that is expected of NiO in the $Fm3m$ space group. An investigation on the impact of the maximum heating temperature on crystallinity was done by comparing the XRD patterns of molten salt synthesis products heated at 300 °C, 400 °C, and 550 °C. Samples from all temperatures showed the same strong peaks as initially noted, however the intensities of the peaks varied. The general
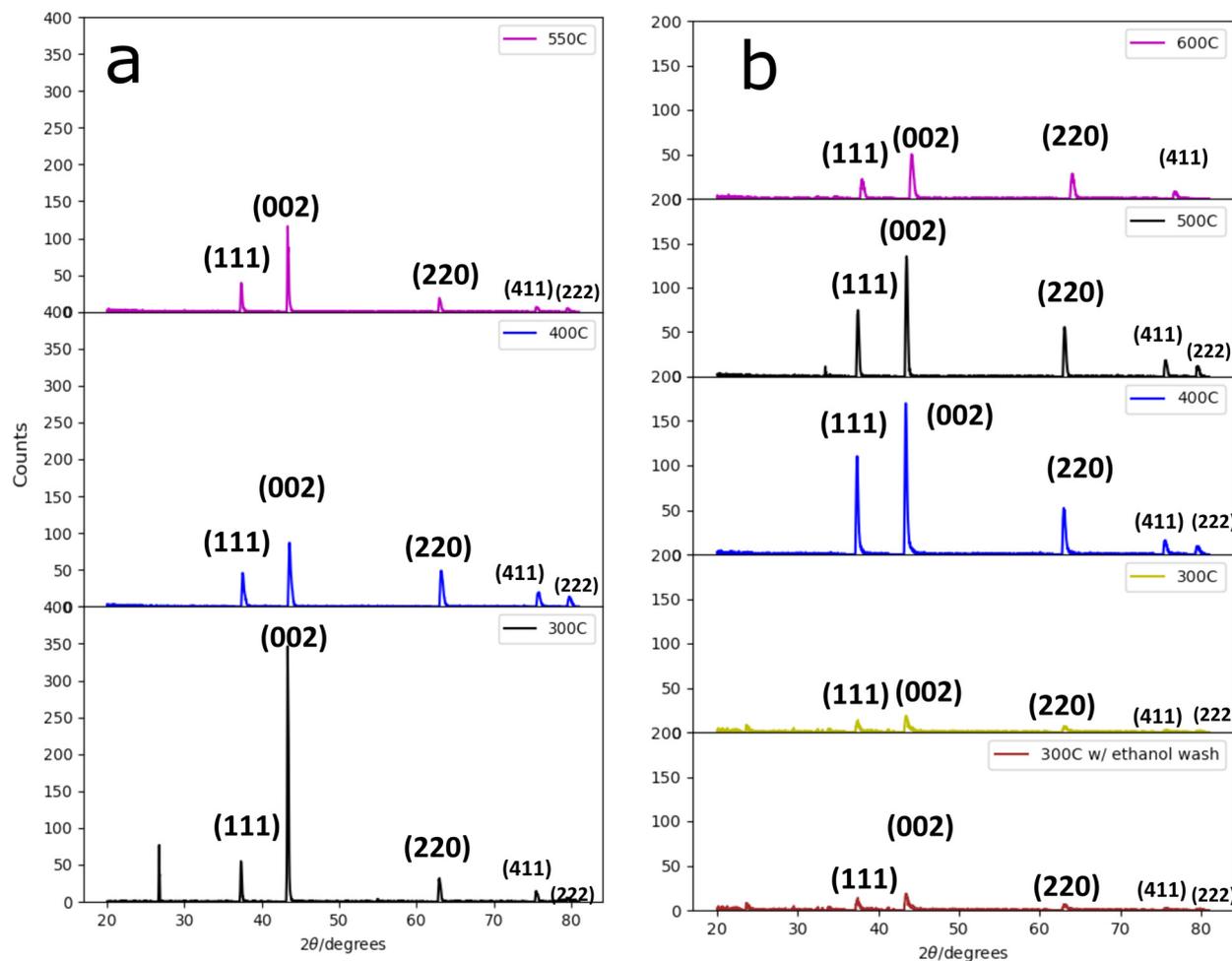

Fig. 1   XRD patterns of initial molten salt synthesis products (a) NiO(100) nanocubes and (b) Li$_2$O-reduced nanoparticles.

trend indicates that the intensities of the peak decrease as calcination temperature increases, with the 300 °C sample showing the highest peaks. Combining this observation with the later observed trend in crystallite sizes indicates that increasing the calcination temperature decreases the average particle size of the system and thus decreases the peak intensity. The exception to this trend is the comparison of the (002) peak between 400 °C and 550 °C where the peak in the 550 °C pattern is the only peak that increases in intensity to be greater than the same peak in the 400 °C pattern rather than decreasing like the other peaks in the 550 °C pattern. One can infer that as the crystallite sizes decrease with increased calcination temperature overall, the crystal plane in the (002) direction for the 550 °C sample resists shrinking as much as the other directions. As the (002) peak is the strongest in all the samples, combining this observation with the cubic shapes observed in TEM imaging leads to the conclusion that these samples grow more pointedly in the (002) direction. An increase in crystallite size with increasing temperature is a trend contrary to what is expected; however, this may be explained through the role of the molten salt mixture. As the melting point for both salts are above 300 °C, thus at 300 °C, the templating effects of the molten salts are likely weak. In contrast, ion adsorption at the surface at higher temperatures may hinder the growth of the crystals. Another standout in this dataset is the presence of a peak in the 300 °C pattern at 26.8° 2θ that can potentially be attributed to graphite. To determine whether the trend in intensities reflected a trend in crystallize sizes, the Scherrer equation was used to calculate the average crystallite size of the five NiO diffraction peaks ((111), (002), (220), (411), and (222)) via peak intensities using integral breadth.[20] The crystallite sizes from the individual peaks are shown in Table S2.† Crystallite sizes derived from the Scherrer equation are given in Table 1: here, one can see the 300 °C sample displays the largest crystallite sizes produced. The samples treated at 550 °C and 400 °C showed overall similar crystallite size despite differences in the peak intensities shown earlier. These results indicate that there is some degree of crystallite shrinkage past 300 °C, but not much in the 400–550 °C range. Comparing the crystallite sizes throughout the different washing steps (Table S1†) performed on the 400 °C sample showed minor change until a vacuum oven drying step was introduced, where the sizes decreased by 5 nm.
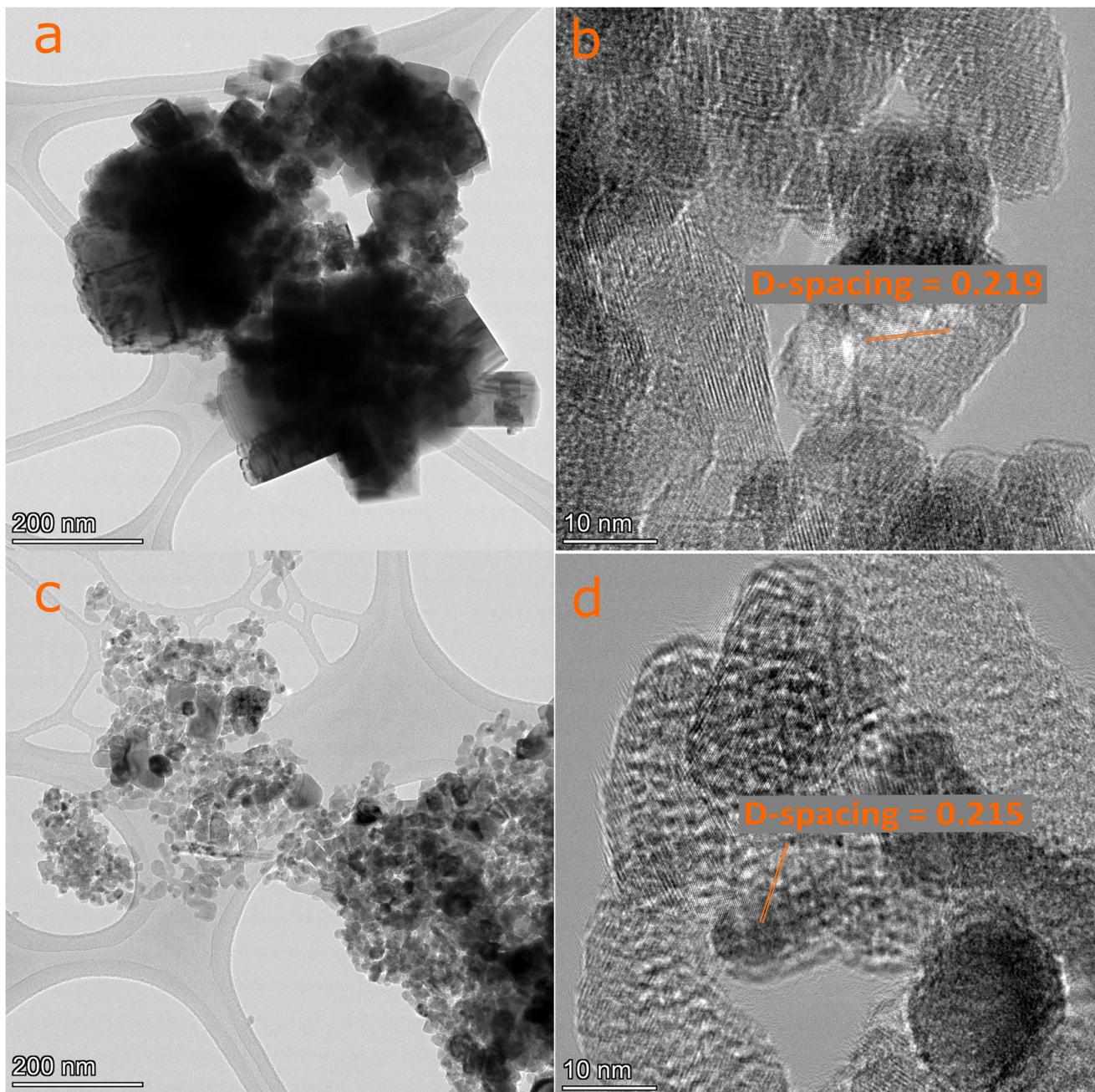
Table 1 Average crystallite sizes of NiO powders derived from the Scherrer formula

Sample/calcination temperature	Crystallite size (nm)
NiO(100) 300 °C	40.9
NiO(100) 400 °C	30.9
NiO(100) 500 °C	27.9
Li$_2$O–NiO 300 °C	22.1
Li$_2$O–NiO 400 °C	18.4
Li$_2$O–NiO 500 °C	12.8
Li$_2$O–NiO 600 °C	15
NiO(111) 500 °C	13.2

XRD analysis of the Li$_2$O-reduced samples (Fig. 1b) provided valuable information on the degree of crystallinity of these samples. While the same 2θ peaks were present in the XRD, the intensity of said peaks significantly decreases. A similar temperature study was done on these samples from 300 °C to 600 °C. As the temperature increased, the peaks gained intensity and slightly narrowed, suggesting that the samples did become more crystalline. Crystallite size analysis shows the order of largest to smallest crystals as 300 °C, 400 °C, 600 °C, then 500 °C, showing a similar trend of larger crystals at lower temperatures but not at higher temperatures. More interestingly, decreasing the synthesis time by removing the 1 h hold after the sample reaches maximum temperature seemed to have a much more direct effect on crystallite size, as 400 °C without the 1 h hold showed the largest crystallite size of the Li$_2$O reduced samples at 31 nm (ESI† Table S1). Li$_2$O was added to molten salt systems in previous literature reports due to Lux–Flood properties (acid–base properties that consist of an acid used as an oxide ion acceptor and base used as the oxide ion donor) being shown to decrease crystallite size;[21] this is reflected in the overall decrease in crystallite size of the Li$_2$O samples versus the initial samples not containing Li$_2$O. Comparison of crystallite sizes of both NiO(100) and Li$_2$O-reduced NiO with NiO(111) was done (Table S2†) to indicate that NiO(111) shows the most consistently small nanoparticles. While the 300 °C Li$_2$O-reduced sample showed the smallest average crystallite size at 11.2 nm, the substantial standard deviation indicates a lack of consistency of the crystalline samples for the polycrystalline powder. In contrast, NiO(111) shows substantially lower standard deviation, indicating consistently small nanoparticles.

TEM imaging on initial molten salt synthesis products shows cubic shaped nanoparticles with significant agglomeration (Fig. 2a and b). The average size of visibly distinct nanocubes outside or at the edge of agglomeration is around 50 nm. HRTEM was integral to determining the presence of NiO(100) and NiO(111) facets through comparing their respective d-spacings, or the spacings measured between lattice fringes seen in the high-resolution magnification range. HRTEM was used to measure the lattice spacings on cubic nanoparticles from the 300 °C calcined sample to determine an average D-spacing of 0.219 nm across several lattice fringes. This corresponds to the (200) lattice fringe.[22] The observed d-spacing measurement of NiO(111) in previous faceted NiO studies was 0.24 nm.[9,14] Thus, the observed (100) d-spacing measurement differs from the (111) measurement by 0.03 nm, indicating that the cubic nanoparticles do contain a different surface facet than the (111) nanosheets. NiO(100) d-spacing measurements (Table S4†) show a standard deviation of 0.014 nm. Confirming different d-spacings between the NiO(100) and NiO(111) sample provides evidence of a difference in surface facet exposure between the molten salt synthesized nanocube and solvothermally produced nanosheet sample.

1452 | *RSC Appl. Interfaces*, 2025, **2**, 1448–1460

© 2025 The Author(s). Published by the Royal Society of Chemistry

Fig. 2 (a and c) TEM images of NiO(100) nanocubes and Li_2O-reduced samples, respectively. (b and d) HRTEM images with lattice measurements of respective samples.

After observing the significant agglomeration present in the initial nanocube (100) samples, alterations to the synthesis were explored to produce finer nanoparticles. Previous work done to investigate the relationship between crystallite size of molten salt systems ($NaNO_3$/KNO_3 in particular) showed that altering the acidity/basicity of the system may decrease the crystallite size by adding Lux–Flood bases.[21] Li_2O was used as a Lux–Flood base and oxygen source in previous molten salt synthesis of NiO systems,[11] thus Li_2O was added to the system to decrease the agglomeration seen in the nanocube system. As such, the

Li_2O-reduced samples showed visible differences via TEM analysis of the 400 °C calcined product, with much finer and more plentiful nanoparticles present in the images (Fig. 2c and d). The size of these finer yet more polycrystalline nanoparticles varied in the 10–100 nm range with larger nanoparticles being typically located in more densely packed regions. The densely packed regions show up darker in TEM images, but the visible separation between nanoparticles in this region indicates that Li_2O-reduced samples show less agglomeration than initial molten salt synthesis samples. While the finer nature and lack of

agglomeration of these nanoparticles is a positive sign, reduced nanoparticles also largely lack the cubic nature of the non-reduced nanocube samples; this puts doubt onto whether the bulk of these samples is in the (100) rock salt crystal facet. For this reason and the varying shapes visible in the images, it is inferred that these nanoparticles are more polycrystalline in nature. Interestingly however, select few areas in the reduced samples showed some crystal lattice fringes where average d-spacing measurement gained from these measurements was 0.21 nm with an even smaller standard deviation of 0.014 (as shown in Table S3†), similar to the (100) nanocubes. This result indicates that while the samples are largely poly crystalline, they do exhibit some degree of NiO(100) character in the sample. This is a positive sign of NiO rock salt character in the Li_2O-reduced samples, even if they are not largely cubic or in the (100) facet. The substantially different properties of the reduced samples are likely due the Lux–Flood base properties of Li_2O allowing the Ni metal ions formed from the dissolution of the precursor to react with the O ions provided by Li_2O inside the molten salt reactor during the heating step.[11] Through this interaction, the temperature of the reaction producing the NiO nanoparticles is decreased. The reaction of metal and oxygen ions is presumably faster than the crystal growth step that ensures the nanoparticles grow in the (100) facet direction. The observations shown in the HRTEM imaging of the Li_2O-reduced samples (Fig. 2b and d) show the synthesis of an unintended polycrystalline product through altering the basicity of the system, a novel discovery formed through attempts to decrease agglomeration of the nanocube samples.

To confirm the presence of NiO nanoparticles throughout the faceted and polycrystalline nanomaterials, STEM-EDS

was used. Elemental distribution maps (Fig. S2† for map including Na and N) were used to determine the presence of contaminants from the heavy molten salt synthesis, with some counts of N and Na present in the maps. There is doubt on the confirmed presence of N and Na, however, due to neither peaks being present in the EDS spectrum (Fig. S3†), in contrast to strong peaks of Ni and O (alongside smaller Cu peaks caused by the copper grid substrate). Investigating the nature of agglomeration on the (100) samples as well led to STEM-EDS analysis of the NiO(100) products (Fig. S2 and S3†). Here, some counts of N, Na and potentially C by-products were initially observed; however, like the polycrystalline sample, no noticeable peaks for any N, Na, or C signal were detected in the EDS spectrum. The elemental maps showing potential N, Na, and C by-products in either sample are most likely due to the counts not being normalized against each other during the scanning process. Throughout the multiple synthetic trials, several different washing procedures were done after the molten salt synthesis to remove potential contaminants (as described in the ESI†). From these observations and procedures, one can infer that the difference between the fine nanoparticles of the Li_2O-reduced samples and the nanocubes is the ability to reduce the magnitude of agglomeration of the nanomaterials (Fig. 3).

X-ray absorption spectroscopy experiments (Fig. S4 and S5†) were done to provide insight into the local electronic and structural differences between the (100) and (111) facets. XAS measurements were done on thin film samples deposited on a glassy carbon electrode both before (-tf) and after potential dynamic electrochemical treatment with a stop potential of 1.7 V $vs.$ RHE (-pd). In Fig. S4,† the Ni K-edge X-ray absorption near-edge structures (XANES) of NiO(100) and
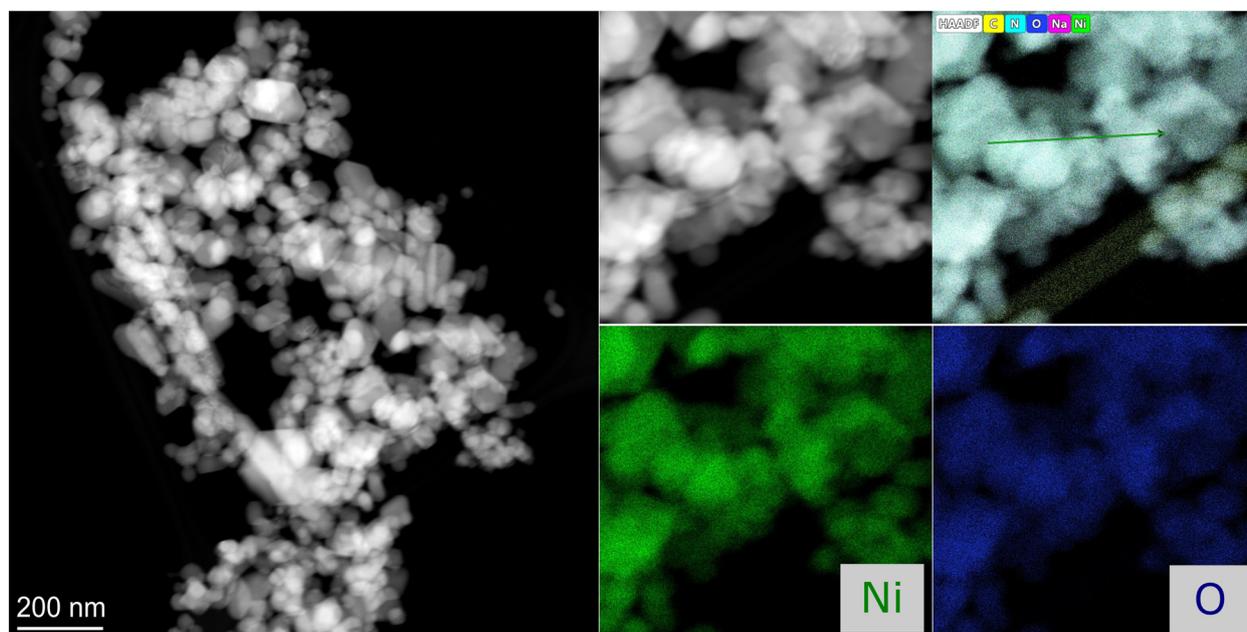

Fig. 3 STEM-EDS elemental dispersion map of Li_2O-reduced NiO nanoparticles.

1454 | *RSC Appl. Interfaces*, 2025, **2**, 1448–1460

© 2025 The Author(s). Published by the Royal Society of Chemistry

NiO(111) are presented and compared with the two commercial reference samples NiO_ROTH and LiNiO₂ with a nominal Ni oxidation state of +2 and +3, respectively. The edge positions (integral method) of NiO(100) and NiO(111) are very close to the NiO_ROTH reference sample (Table S5†), indicating the bulk oxidation state close to +2. Fourier transform of the EXAFS of NiO(100) and NiO(111) exhibits the two prominent peaks corresponding to the Ni–O and Ni–Ni coordination path, as shown in Fig. S5.† A similar peak position and shape associated with NiO(100) and NiO(111) signifies no observable structural differences. Overall, XANES and EXAFS analysis of the Ni k-edge position showed negligible differences in the edge position and Ni–O and Ni–Ni peak positions between the NiO(100) and (111) samples, indicating similar local electronic and environmental difference between the different faceted samples. Both materials exhibit the characteristic EXAFS of rock salt NiO. Similarly, no substantial difference in the edge energies was observed in between (-tf) and (-pd) samples of both faceted samples. These findings indicate that while the nanocube and nanosheet samples show physical differences in their lattices and level of agglomeration, the NiO products retain similarities in electronic states across different synthetic techniques and electrochemical treatment. Structural characterization through XRD and TEM was done on NiO(111) nanosheets in previous synthetic studies.[9,13] The defining structural characteristics of these nanosheets include identical XRD peak patterns to the NiO(100) and polycrystalline NiO patterns (with peaks corresponding to (111), (002), (220), (411), and (222) rock salt crystal planes), and sheetlike structures observed in TEM with diameters up to 1 μm and thickness of 1–5 nm.[13] The most notable physical characterization seen in TEM imaging is hexagonal holes present in the nanosheets with diameters of 20–100 nm; electron diffraction patterning on these holes indicates the presence of (111) planes parallel to the main nanosheet surface within these hexagonal holes. Finally, while both NiO(100) and Li₂O-MSS NiO samples have shown signs of significant agglomeration, TEM imaging of NiO(111) shows fine non-agglomerated nanosheets. The fine nanosheets shown in TEM imaging in combination with smaller crystallite sizes from the Scherrer equation provide evidence of a lack of agglomeration for the NiO(111) samples.

After thorough structural characterization, the OER catalytic activity was measured through RDE experimentation (Fig. 4). RDE testing on a polished Au substrate was used in this study as it is a well-established and defined technique with the additional benefit of avoiding contamination issues seen with using porous carbon substrates (GDL).[17] The three sets of samples that were evaluated include NiO(111) nanosheets from the solvothermal synthesis as a baseline, the NiO(100) nanocubes synthesized from the initial molten salt route (NiO(100)), and the NiO nanoparticles from the Li₂O-reduced synthesis (Li₂O-MSS NiO). An important initial observation is the difference in ink dispersion between NiO samples with different facets and synthesis techniques. The NiO(111) samples produced from established synthetic methods were used as a baseline for OER measurements, with the ink prepared from these samples dispersing very evenly and readily in the DI/IPA/Nafion solvent. In contrast, NiO(100) samples produced from the initial molten salt synthesis dispersed unevenly and settled within ten minutes of ink preparation. The lack of dispersion most likely led to problems with catalyst properly covering the working electrode surface in the thin film form and thus prevented electrochemical active sites from being easily accessible. This
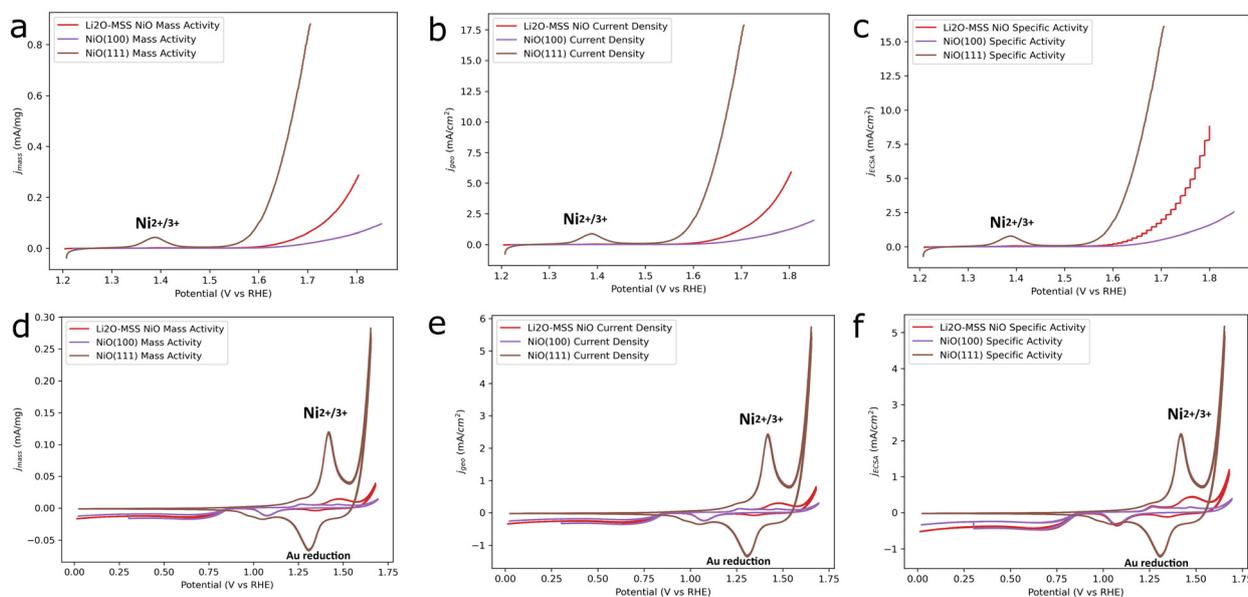

Fig. 4 Linear sweep voltammograms (top) and cyclic voltammograms (bottom) of Li₂O-MSS NiO, NiO(100), and NiO(111) nanomaterials. Current trends were evaluated through mass activity (a and d), current density (b and e), and specific activity (c and f).

also leads to the catalyst loading becoming less defined than the intended calculated loading, as our calculation assumes homogenous dispersion of particles in the pipette tip and then on the electrode surface. This is likely a result of significant agglomeration in the nanocube sample. In order to improve the lack of dispersion and aid in reproducibility, different catalyst ink formulas were used to optimize ink activity: initial OER tests were done using an ink formula with a 17.8 μg cm⁻² catalyst loading (labelled Ink Formula A in the ESI†) based on previous studies showing high catalyst utilization at low loadings which helped avoid electrode bulk complications.[17] Catalyst delamination (detachment of the catalyst from the electrode surface) is typically less of a problem at lower loadings due to low loadings having the advantages of fewer sites lost to catalyst layer thickness, lower current and complications from the counter electrode or shifting local pH, and less bubble entrapment. Lower loadings face the drawbacks of lower current and potential working substrate contributions to activity and CVs, thus for qualitative activity comparison between the NiO electrocatalysts, another formula with a 100 μg cm⁻² loading (labelled Ink Formula B in the ESI†) was used for the RDE experiments shown in this paper. While the dispersion slightly improved with Ink Formula B, the same general electrochemical trend (significantly lower current density) was seen across ink formulas. Finally, the most interesting is that NiO samples produced from the Li₂O-reduced molten salt synthesis suspend much more readily and uniformly in the ink solution, thus making a much homogeneous ink. Linking this observation with the agglomeration seen in HRTEM, the improved dispersion ability of the Li₂O-reduced sample is likely linked with the lessened agglomeration seen with the finer nanoparticles. Linear sweep voltammetry (Fig. 4a–c) and cyclic voltammetry (Fig. 4d–f) were conducted to investigate the current trends and reproducibility of each electrocatalyst sample. LSVs and CVs were conducted before and after an activation step of 350 CV cycles at 250 mV s⁻¹. The comparison of before and after the 350 cycles can be seen in Fig. S6.† One notable difference between the samples is the presence of a smaller peak at ~1.25 V in the NiO(100) and Li₂O-MSS samples that is not present (or at least much less obvious) in the NiO(111) sample. This small peak may come from the Au electrode substrate, which has been shown to have oxidation peaks at ~1.2 and ~1.5 V vs. RHE.[23] An RDE experiment using the same parameters of the NiO studies was done on a bare Au substrate electrode to highlight the presence of the Au redox peaks, as exhibited in Fig. S10.† The absence of the Au oxidation peak in the (111) sample is of interest, as it implies that the higher performing nanosheets are covering up the Au oxidation. This is likely through the better coverage of NiO(111) on the electrode due to improved ink rheology. More extensive durability testing was done through potentiostatic hold tests on the NiO materials at 1.6 V for 2 h, depicted in Fig. S7.† These potentiostatic studies indicated that NiO(111) maintains the best stability with a current of around 45 mA cm⁻² held over

the 2 h period, followed by Li₂O-MSS with a current around 22 mA cm⁻², and finally NiO(100) that sees its current drop down to 0 mA cm⁻² over the two hours. The reproducibility trends for LSV and CVs can be seen in Fig. S8 and S9,† respectively. While all the samples show some degree of substantial variation in reproducibility, NiO(100) showed the most consistent reproducibility the three trials measured, followed by NiO(111) and Li₂O-MSS NiO with equal reproducibility. This trend is interestingly opposite to the ink stability. The larger range of variation for Li₂O-MSS may be because of the polycrystalline nature of the sample in contrast to the more ordered NiO(111) and (100) which further affects ink rheology and electrode preparation. LSV analysis between the three samples reveals the most obvious result with these samples, that is, a substantial decrease in current density (current normalized to geometric area of the Au electrode (0.196 cm²)) of both NiO(100) nanocubes and Li₂O-MSS samples in comparison to the baseline NiO(111) samples. One can immediately notice that both NiO(100) and Li₂O-MSS NiO samples fail to reach 10 mA cm⁻², which is typically the benchmark for OER electrodes at low current density.[4,24] The average LSV current density for these samples was evaluated at 1.55 V (a metric used in similar low current density studies)[1,17] in Table 2 where it is evident that both NiO(100) and Li₂O-MSS NiO have average current densities an order of magnitude lower than NiO(111), indicating that these samples are less ideal catalysts for the OER (as the nominal loading was identical). While still being noticeably less active than NiO(111), Li₂O-MSS NiO does show substantial improvement in electrode activity over the NiO(100) samples.

An additional observation is the presence of oxygen reduction peaks in the NiO(100) CVs below 0.75 V, which may point to O₂ sticking to the surface despite the constant N₂ bubbling. This phenomenon would lead to a large reduction in the number of active sites in comparison to NiO(111). In contrast, the lack of oxygen reduction in the NiO(111) CVs indicates that O₂ more readily detaches, thus no ORR is observed. These observations indicating a potentially reduced number of active sites most likely play a role in the decreased activity of both (100) and Li₂O-MSS NiO (which also shows oxidation below 0.75 V). The trend of NiO(111) > Li₂O-MSS > NiO(100) is further reflected in alternative normalizations of the current, namely in mass activity (normalizing the current to metal oxide catalyst mass) (Fig. 4a and d) and specific activity (Fig. 4c and f). Steps are present in some LSV scan (Fig. 4c) due to the nature of the potentiostat measurements, where several current values are taken at each potential. This may lead to

Table 2 Comparing average densities at 1.55 V ability of NiO(100)

Sample	Average current @ 1.55 V	Current st. dev
Li₂O–NiO	0.0327	0.0175
NiO(100)	0.0182	0.0013
NiO(111)	0.2622	0.1869

Table 3 Double layer capacitance (C_{DL}), electrochemical surface area, and Tafel slope measurements of NiO electrocatalysts

Sample	C_{DL} (µF)	ECSA (cm^2)	Tafel slope (mV dec^{-1})
Li$_2$O–NiO	5.25	0.131	373
NiO(100)	6.04	0.151	1270
NiO(111)	7.86	0.197	48.2

noisy data depending on the magnitude of the varying current. While both NiO(100) and Li$_2$O-MSS lag behind NiO(111) in all categories, it is interesting to note that there seems to be an improvement in the specific activity comparison, more noticeably for the Li$_2$O-MSS samples. The observation that normalizing current to ECSA (displayed in Table 3) shows improved activity leads to interesting results when linked with the presence of significant agglomeration in HRTEM for NiO(100) and decrease in current when normalized for mass. If the specific activity is an accurate reflection of the electrochemical surface area, the improved activity indicates that not all the mass being used to normalize the current or the geometric surface area of the electrode is electrochemically active, thus negatively impacting the catalyst OER activity determination. This would correspond with the agglomeration seen in TEM imaging and the issues seen with ink dispersion. In the case of ink dispersion, the Li$_2$O-reduced samples produced finer nanoparticles and further dispersion of the agglomerating nanoparticles likely aided in the NiO catalyst powders successfully dispersing into the ink.

However, it is important to note that the accuracy of the double layer capacitance measurements should be scrutinized, as the capacitance of metal oxides is known to be difficult to reliably measure.[14,18] Capacitance values can be seen in Table 3, where these values were derived from the capacitance plots shown in Fig. S11.†

The activity trend is further reflected in the cyclic voltammetry measurements with NiO(111) being the highest performing catalyst (Fig. 4 and 5). Cyclic voltammograms

are shown at 50 mV s^{-1} (Fig. 4d–f) to more readily determine peak potentials, and 10 mV s^{-1} (Fig. 5a) for higher magnitude currents. The most interesting observation made when comparing the CVs of the three sets of samples is the shift in peak potentials between them. All three samples show a noticeable peak around 1.4 V, which typically corresponds to the Ni$^{2+\rightarrow3+}$ range.[4] While having the highest current across the different normalizations, NiO(111) has a Ni^{2+} peak position in between the two other samples: Li$_2$O-MSS NiO shifts the potential to the right, while NiO(100) shifts it to the left. It is easy to speculate whether the shift in potential is directly related to the smaller (potentially Au substrate) peak present at ~1.25 V in (100) and Li$_2$O-MSS that is not present in the (111) sample. Interestingly, the onset potential for the rest of the OER range shifted further to the left for NiO(111), indicating a lower overpotential (which matches well with its overall superior activity as an electrocatalyst). The shifts in Ni^{2+} peaks for the poorer performing samples provide an interesting question as to whether there is a shift in reaction mechanism for both samples. This further begs the question of whether the shift in mechanism is a result of the different faceted NiO nanoparticles because of the available active sites, or if the significant agglomeration has an effect. To the later point, it is noted that Li$_2$O-MSS NiO shifts in the opposite direction of NiO(100) with lessened agglomeration. Finally, Tafel plot analysis (slopes given in Table 3) reflects the activity trend of (111) > Li$_2$O-MSS > (100) through (111) showing the smallest Tafel slope (Fig. 5b) by several orders of magnitude. NiO(111) shows a Tafel slope of 48.2 mV dec^{-1} which is consistent with previously reported values for the electrocatalyst;[14] however, the jump in magnitude for Li$_2$O-MSS (373 mV dec^{-1}) and NiO(100) (1270 mV dec^{-1}) reflects the decrease in catalytic activity for the newly synthesized samples. Looking at the Tafel plots (Fig. S12†) provides evidence of mechanism changes, as the rise in slopes occurs at varying potentials in the lower potential range. Observing the changes in slope at
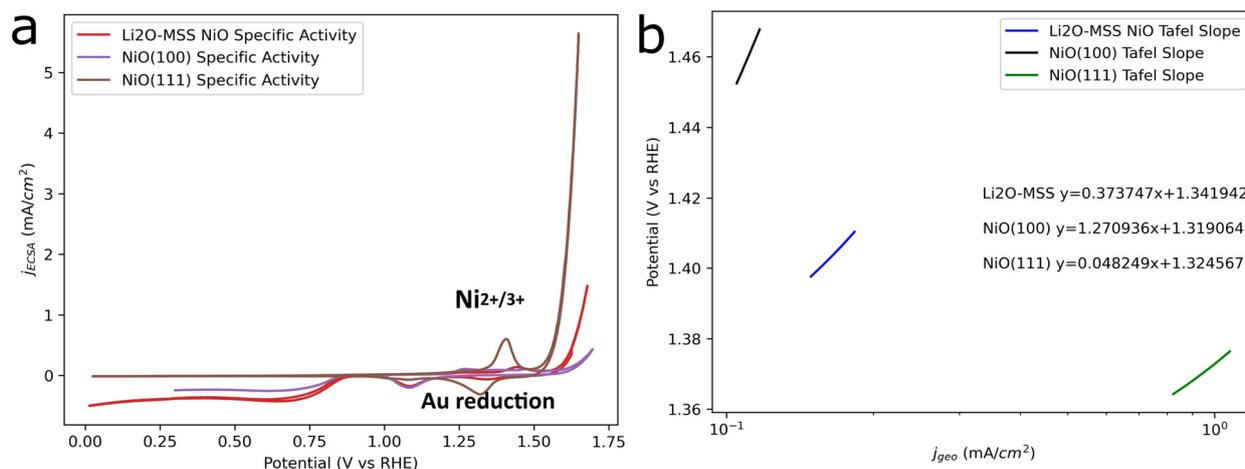
Fig. 5 (a) Cyclic voltammograms at 10 mV s^{-1} scan rate. (b) Tafel slopes calculated at low (<3 mA) current densities.

© 2025 The Author(s). Published by the Royal Society of Chemistry

RSC Appl. Interfaces, 2025, **2**, 1448–1460 | **1457**

the same area of the Tafel slopes indicates a change in the kinetics of the rate-determining step, likely due to the overpotential of one intermediate coupled to the Ni(II) oxidation. HRTEM imaging was done on the synthesized NiO(100) and Li$_2$O-MSS NiO samples after RDE testing as seen in Fig. S14.† Samples were collected by sonicating the ink-deposited Au electrode in IPA for five minutes, and TEM grids were prepared by sonicating the sample-containing IPA solvent for 30 minutes then depositing on the copper TEM grid. HRTEM imaging through the different magnitudes (17 500×, 58 000×, and 74 000×) shows potential morphological changes in the samples after the electrochemical testing as they show more amorphous character. One should take caution in the conclusions taken from these initial post-OER images, however, as the low loading of the catalyst on the electrode led to difficulty in employing the NiO material for TEM preparation. Further post-electrochemical testing should be done on electrodes with a higher catalyst loading to gain more insight into the morphology of the tested NiO systems.

In discussion, the substantial decreases in activity for NiO(100) and Li$_2$O-MSS compared to NiO(111) present interesting questions about structure–activity relationships for our NiO electrocatalyst systems. Previously, DFT calculations were used to indicate that the NiO(100) surface should show decreased overpotentials in comparison to the (111) surface;[8] this conclusion came from the observation that the NiO(100) surface showed decreased reaction free energy throughout the four-electron reaction pathway, with a large drop off in reaction free energy difference in the OOH intermediate step. While this should ideally lead to improved overpotentials due to the OOH intermediate step corresponding to the NiOOH active phase of our NiO electrocatalysts, it is important to point out large assumptions made in the DFT calculation in contrast to the experimental work done here. Namely, the calculation was done in a vacuum space of 18 Å along the non-periodic direction (in sharp contrast to the constantly N$_2$-bubbled electrolyte of the RDE system) and the reaction free energy calculation was done at the applied potential of 1.57 V vs. RHE, in contrast to a constantly cycling potential in a kinetic RDE experiment. These differences in the calculation of NiO(100) surface energy represent the large gap between theoretical calculations and the largely dynamic nature of the electrocatalytic system. Investigations into faceted LaNiO$_3$ revealed improved OER activity for the (111) facet due to the surfaces' ability to form a more active oxyhydroxide, an observation that shares similarity with the findings in this study.[25] A similar trend of larger peaks at 1.4 V for the (111) sample and smaller peaks for the (100) was observed. A common note on both trends is the understanding of a hydroxide layer forming on top of the NiO catalyst, an idea that may not have necessarily been accounted for in DFT calculations.[26] Additional post-catalysis characterization such as Raman spectroscopy, pXRD pattern analysis, and SEM/ TEM imaging is still needed to confirm the existence of

significant morphological changes throughout the different catalyst. This analysis could be used to further elucidate any mechanistic differences to explain the observed activity trend. An additional factor potentially neglected in DFT calculations is the semiconductor nature of NiO which causes charge transfer to rely on band structure.[27] Additionally, it should be noted that other previously done studies of NiO facets for electrocatalysts have also shown NiO(100) as the least active surface facet, likely for similar reasons to those observed in this study.[10]

An additional hypothesis on the decrease in activity is the difference between wet chemical synthesis routes and the solid-state routes used to synthesize the two new samples. Previous attempts to synthesize NiO(100) in wet chemistry have been unsuccessful due to the (111) facet being more thermodynamically stable in wet chemistry environments.[28] This stability was further corroborated by *ab initio* calculations that showed NiO(100) having a cleavage energy of 5.34 J m^{-2} in contrast to the 0.99 J m^{-2} of hydroxylated NiO(111).[9] If the cleavage energy of NiO(100) is this high, it may not be able to properly disperse in the ink preparation step and thus struggle to properly cover the Au electrode. The lack of availability of its electrochemically active sites thus prevents it from showing any OER activity. This provides an interesting insight into how the properties of solid-state chemistry may directly affect the wet chemical nature of water electrolysis. To probe this, a study should be done on the electrochemical activity of NiO(100) nanocubes in an electrochemical set-up that allows it to retain its catalyst powder form to confirm if better activity is shown in the solid state, such as the single particle electrochemistry that was done on Co$_3$O$_4$ nanoparticles.[29]

Conclusions

NiO nanomaterials of different surface facets and crystalline natures were successfully synthesized and tested for OER activity. NiO nanocubes with increased (100) facet exposure (NiO(100)) and polycrystalline NiO (Li$_2$O-MSS) were synthesized through a facile molten salt synthesis technique, the latter of which is a newly developed approach to produce very fine polycrystalline nanoparticles through altering the basicity of the system with a Lux–Flood base (Li$_2$O). While both samples showed decreased activity compared to the established NiO(111) nanosheets they were tested against, the improvement in activity of the polycrystalline NiO over the nanocube NiO(100) provides unexpected insight into how different crystalline properties can be used to improve electrocatalytic activity. However, the difficulties of this synthesis come to light with evidence of substantial agglomeration of the polycrystalline and nanocube products shown through STEM-EDS. The decreasing activity trend of (111) > Li$_2$O-MSS > (100) differing from some initial speculations of highly active (100) is likely rooted from three causes: the different experimental conditions between the initial DFT calculations done under vacuum and a dynamic

RDE system, the difficulties of the nanocube system dispersing in ink, and the significant agglomeration seen in the nanocube and polycrystalline samples.

Understanding particle faceting and the impact on OER reactivity is critical to developing catalyst design principles. Catalyst design is critical in AEM electrolysis due to the efficiency limitations. Efforts in NiO (and stoichiometric oxides) are particularly important in the AEM/OER in that oxides aim to mimic electrode conditions and thermodynamically favored states of the catalyst under those conditions. These types of studies address the limitations of a historical focus on sub stoichiometric oxides, which haven't been particularly enabled in AEM-LTE. Understanding faceting and reactivity is important across a wider range of technologies, particularly different electrochemical energy conversion approaches.

Data availability

All data available upon request to corresponding author.

Author contributions

Hayes, D. W.: wrote original draft, investigation, data curation, software, formal analysis, and validation. Brim, E., Ruecker, K., Taffa, D. H, and Bisen, O.: support in synthesis, data curation, software, formal analysis and validation. Alia, S., Risch, M., Lorenz, J., Harms, C., Wark, M.: supervision, project administration, and resources. Richards, R.: conceptualization, project administration, and supervision. Paper was reviewed and edited by all participants.

Conflicts of interest

The authors declare no financial or personal conflicts of interest in the work reported in this paper.

Acknowledgements

Notes and references

1 E. K. Volk, S. Kwon and S. M. Alia, *J. Electrochem. Soc.*, 2023, **170**, 064506.

2 N.-T. Suen, S.-F. Hung, Q. Quan, N. Zhang, Y.-J. Xu and H. M. Chen, *Chem. Soc. Rev.*, 2017, **46**, 337–365.

3 Y. Liu, D. Zhou, T. Deng, G. He, A. Chen, X. Sun, Y. Yang and P. Miao, *ChemSusChem*, 2021, **14**, 5359–5383.

4 D. Hayes, S. Alia, B. Pivovar and R. Richards, *Chem Catal.*, 2024, **4**, 100905.

5 B. Zhang, X. Shang, Z. Jiang, C. Song, T. Maiyalagan and Z. J. Jiang, *ACS Appl. Energy Mater.*, 2021, **4**, 5059–5069.

6 J. Wang, J. Xu, Q. Wang, Z. Liu, X. Zhang, J. Zhang, S. Lei, Y. Li, J. Mu and E.-C. Yang, *Phys. Chem. Chem. Phys.*, 2022, **24**, 6087–6092.

7 G. Yang, H. Xiang, M. Rauf, H. Mi, X. Ren, P. Zhang and Y. Li, *J. Power Sources*, 2021, **481**, 228925.

8 T. Sun, D. Wang, M. V. Mirkin, H. Cheng, J. C. Zheng, R. M. Richards, F. Lin and H. L. Xin, *Proc. Natl. Acad. Sci. U. S. A.*, 2019, **116**, 11618–11623.

9 C. A. Cadigan, A. R. Corpuz, F. Lin, C. M. Caskey, K. B. H. Finch, X. Wang and R. M. Richards, *Catal. Sci. Technol.*, 2013, **3**, 900–911.

10 R. Poulain, A. Klein and J. Proost, *J. Phys. Chem. C*, 2018, **122**, 22252–22263.

11 T. Li, Y. Xu, X. Qian, Q. Yue and Y. Kang, *ACS Appl. Energy Mater.*, 2020, **3**, 3984–3990.

12 M. D. Susman, H. N. Pham, X. Zhao, D. H. West, S. Chinta, P. Bollini, A. K. Datye and J. D. Rimer, *Angew. Chem., Int. Ed.*, 2020, **59**, 15119–15123.

13 J. Hu, K. Zhu, L. Chen, H. Yang, Z. Li, A. Suchopar and R. Richards, *Adv. Mater.*, 2008, **20**, 267–271.

14 D. H. Taffa, E. Brim, K. K. Rücker, D. Hayes, J. Lorenz, O. Bisen, M. Risch, C. Harms, R. M. Richards and M. Wark, *ACS Appl. Mater. Interfaces*, 2024, **16**, 62142–62154.

15 D. M. Többens and S. Zander, *J. Large-Scale Res. Facil.*, 2016, **2**, A49.

16 O. Y. Bisen, M. Baumung, M. Tatzel, C. A. Volkert and M. Risch, *Energy Adv.*, 2024, **3**, 504–514.

17 S. M. Alia and G. C. Anderson, *J. Electrochem. Soc.*, 2019, **166**, F282.

18 D. M. Morales and M. Risch, *JPhys Energy*, 2021, **3**, 034013.

19 Z. Y. Yu, Y. Duan, X. Y. Feng, X. Yu, M. R. Gao and S. H. Yu, *Adv. Mater.*, 2021, **33**, 1–35.

20 A. L. Patterson, *Phys. Rev.*, 1939, **56**, 978–982.

21 Y. Du, P. Rogers and D. Inman, *J. Mater. Sci.*, 1996, **31**, 3361–3364.

22 S. Visweswaran, R. Venkatachalapathy, M. Haris and R. Murugesan, *Appl. Phys. A: Mater. Sci. Process.*, 2020, **126**, 524.

23 A. R. Silva Olaya, B. Zandersons and G. Wittstock, *ChemElectroChem*, 2020, **7**, 3670–3678.

24 C. C. L. McCrory, S. Jung, J. C. Peters and T. F. Jaramillo, *J. Am. Chem. Soc.*, 2013, **135**, 16977–16987.

25 A. Füngerlings, M. Wohlgemuth, D. Antipin, E. van der Minne, E. M. Kiens, J. Villalobos, M. Risch, F. Gunkel, R. Pentcheva and C. Baeumer, *Nat. Commun.*, 2023, **14**, 8284.

26 M. Mattinen, J. Schröder, G. D'Acunto, M. Ritala, T. F. Jaramillo, M. B. Stevens and S. F. Bent, *Cell Rep. Phys. Sci.*, 2024, **5**, 102284.

27 D. Antipin and M. Risch, *JPhys Energy*, 2020, **2**, 032003.

28 A. Wander, I. J. Bush and N. M. Harrison, *Phys. Rev. B: Condens. Matter Mater. Phys.*, 2003, **68**, 233405.

29 Z. Liu, H. M. A. Amin, Y. Peng, M. Corva, R. Pentcheva and K. Tschulik, *Adv. Funct. Mater.*, 2023, **33**, 2210945.